Electrical Impedance Tomography Guided by Digital Twins and Deep Learning for Lung Monitoring

Liying Zhu, Wu Lu, *Member, IEEE,* Manuchehr Soleimani, Zhe Li, Maomao Zhang, *Member, IEEE*

***Abstract*— In recent years, there has been an increasing interest in applying electrical impedance tomography (EIT) in lung monitoring, due to its advantages of being non-invasive, non-ionizing, real-time, and functional imaging with no harmful side effects. However, the EIT images reconstructed by traditional algorithms suffer from low spatial resolution. This paper proposes a novel EIT-based lung monitoring scheme by using a 3D digital twin lung model and a deep learning-based image reconstruction algorithm. Unlike the static numerical or experimental simulations used in other data-driven EIT imaging methods, our digital twin lung model incorporates the biomechanical and electrical properties of the lung to generate a more realistic and dynamic dataset. Additionally, the image reconstruction neural network (IR-Net) is used to learn the prior information in the dataset and accurately reconstruct the conductivity variation within the lungs during respiration. The results indicate that EIT using a guided digital twin and deep learning-based image reconstruction has better accuracy and anti-noise performance compared to traditional EIT. The proposed EIT imaging framework provides a new idea for efficiently creating labeled EIT data and has potential to be used in various data-driven methods for electrical biomedical imaging.**

***Index Terms*—Electrical impedance tomography, lung modeling, lung imaging, digital twins, deep learning**

I. Introduction

The continuous monitoring of the lung is necessary in the intensive care unit and for accurate pathological diagnosis of lung diseases. Computed tomography (CT) is the routine imaging method used to assess lung aeration, but critically ill patients in emergency situations must be transported to a radiology facility, resulting in radiation exposure and making it unsuitable for continuous lung condition monitoring [1]. Electrical impedance tomography (EIT) is an emerging non-invasive and radiation-free imaging method that has been successfully used to monitor regional lung function in real-time at the bedside, enabling clinical decision making with CT images. EIT reconstructs the variation of conductivity within the human body by applying safe electric currents through electrodes on the body surface and measuring the voltages [2-4]. However, the inverse problem in EIT image reconstruction is highly ill-posed, limiting the spatial resolution of EIT images. To improve spatial resolution, data-driven methods have been introduced in recent years. *Liu et al.* [5-7] proposed a series of sparse Bayesian learning methods to efficiently solve the inverse problem of EIT by exploiting the structured sparsity in the conductivity distribution. As for absolute EIT imaging, *Hamilton et al.* [8, 9] reported the deep D-bar method based on convolutional neural networks that can lead to sharp and reliable reconstructions even for the highly nonlinear inverse problem of EIT. Besides, *Seo et al.* [10] used a variational autoencoder to learn prior information from training datasets, converting the ill-posed problem in EIT image reconstruction into a well-posed one, and validating the effectiveness and feasibility of their approach through numerical simulations. *Ren et al.* [11] proposed a two-stage deep learning method that can achieve high accuracy shape reconstructions with strong robustness. *Zhang et al.* [12] developed a supervised descent learning algorithm for thoracic EIT, which is effective for image reconstruction of EIT and can accelerate the imaging time.

Data-driven methods have shown great potential in the field of lung EIT. By training, prior information in the dataset can be integrated into data-driven algorithms to improve imaging results. Therefore, the quality of the dataset is essential for the performance of data-driven methods. However, obtaining labeled training data for EIT is difficult in practice, so simulation data is commonly used to train networks, such as the 2D data created from 2D chest CT scans [11, 13, 14] and the phantom images with random ellipses [12, 15]. One way to collect more accurate labelled data is building 3D thorax model from CT images [16]. However, using this method is time-consuming as it requires repeated extraction and postprocessing of lung states during the dynamic respiratory process from CT images. Additionally, the number of available 4D chest CT datasets is currently limited, making it difficult to collect

Liying Zhu is with the Department of Biomedical Engineering, City University of Hong Kong, Kowloon, Hong Kong SAR, China (e-mail: liyingzhu3-c@my.cityu.edu.hk).

Wu Lu is with the School of Electrical Engineering, Shanghai University of Electric Power, Shanghai, 200090 China (e-mail: wuluee@shiep.edu.cn).

Manuchehr Soleimani is with the Department of Electronic and Electrical Engineering, University of Bath, Bath BA2 7AY, U.K. (e-mail: M.Soleimani@bath.ac.uk).

Zhe Li is with the Department of Critical Care Medicine, Renji Hospital, School of Medicine, Shanghai Jiao Tong University, Shanghai, 200001 China (email: slamy1987@126.com)

Maomao Zhang is with Tsinghua Shenzhen International Graduate School, Shenzhen, 518055 China. (Corresponding author e-mail: zhangmaomao@sz.tsinghua.edu.cn).

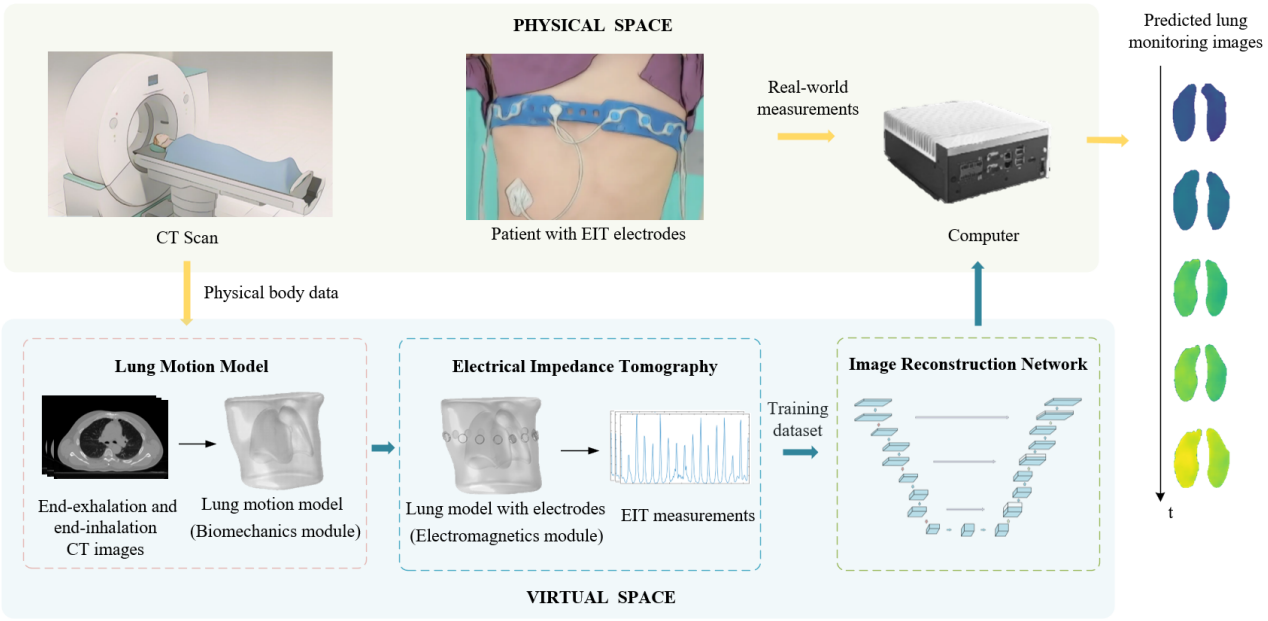

Fig. 1 The proposed imaging framework.

sufficient data for training data-driven algorithms.

Digital twin technology, which uses real-world data to create a virtual replica of physical objects, has been rapidly growing in popularity, particularly in the medical field [17-19]. By using digital twin models, dynamic changes in objects can be accurately predicted, which has been used for multiphase flow imaging by electrical tomography [20]. This technology is expected to have the ability to create labeled lung EIT data more efficiently. In this paper, we build digital twin models of lungs that incorporate both biomechanics and electric fields to enrich the dataset for data-driven algorithms. The first step is building the digital twin lung models in biomechanical field, which is a proved method to formulate respiratory motion and predict the process of lung ventilation effectively in radiation therapy [21-25]. The geometry is built from 3D CT images, and the motion of the lung can be predicted by the finite element analysis (FEA) after solving the corresponding discretized equations. The second step is to set the electrical properties for the lung and adding the electrodes around the thorax in electric field. Then, after injecting electric current through the electrodes, the voltage measurements of EIT during the dynamic respiratory process can be simulated based on the digital twin model. This allows us to create a lung EIT dataset with labeled electrical properties and geometry information for use in data-driven image reconstruction methods.

In this paper, we propose a framework that uses digital twin models to create training datasets and deep learning-based image reconstruction networks to reconstruct EIT images. This framework has two main advantages:

1) Using digital twin lung models to create the dataset allows us to collect more simulated data from limited CT images and provide a new way to create labeled data that is closer to reality. Additionally, the lung models are built based on CT images at end-exhalation and end-inhalation, rather than on the entire 4D CT scan, which reduces radiation exposure for patients compared to using 4D CT images.

2) The proposed image reconstruction network (IR-Net) is designed based on the U-Net structure and is trained on the dataset created by the digital twin lung models. Using IR-Net, lung EIT images can be obtained without requiring a patient's specific sensitivity matrix. It should be noted that other data-driven methods can also adopt the proposed imaging framework. In this paper, the IR-Net structure has been selected because its better performance when limited data is available.

The rest of the paper is organized as follows: Section II introduces the imaging framework, Section III describes the dataset and training details of the network, Section IV discusses the reconstruction results, and Section V presents conclusions and future work.

II. METHODOLOGY

A. Method Overview

The proposed framework contains three main parts, as shown in Fig. 1. First, end-exhalation and end-inhalation CT images from a real-world CT scan are used to generate a lung motion model. Once EIT electrodes are added to the model and the electrical properties are set up, the complete digital twin model is established and the voltage measurements during the respiratory process can be simulated. By building adequate digital twin lung models, a virtual dataset consisting of EIT measurements and corresponding lung information can be generated and used for network training. Through the proposed image reconstruction network, more accurate predicted images for lung monitoring can be obtained based on real-world measurements.

B. Lung Motion Model

The respiratory motion is modeled as a contact problem in this paper. According to [26], the limiting geometry from end-

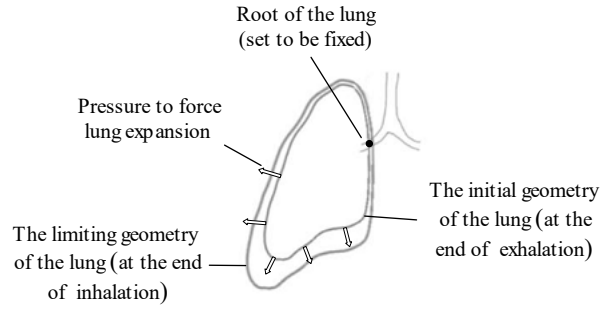

Fig. 2 Illustration of the respiratory motion model

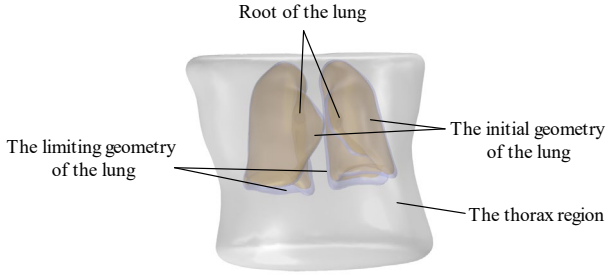

Fig. 3 The geometry of the respiratory motion model

inhalation CT images are used as contact conditions to constrain the expansion of the lung (shown in Fig. 2). A uniform negative pressure is applied to the lung surface to make the lung expand until it fills the limiting geometry. The root of the lung is assumed to be fixed during the breathing.

1) Segmentation

The 3D CT images are segmented using **3D Slicer**, an open source software platform for medical and related imaging research [27]. Taking the influence of other organs, such as the heart, into consideration can improve the modeling accuracy. However, this paper focuses on reconstructing the images of lungs, thus only the region of the lungs was segmented.

The lung segmentations from the end-inhalation CT images and end-exhalation CT images are used to formulate the contact problem. Besides, the thorax of end-exhalation CT images is segmented to indicate the thorax region. The geometry model formed by the segmentations is showed in Fig. 3.

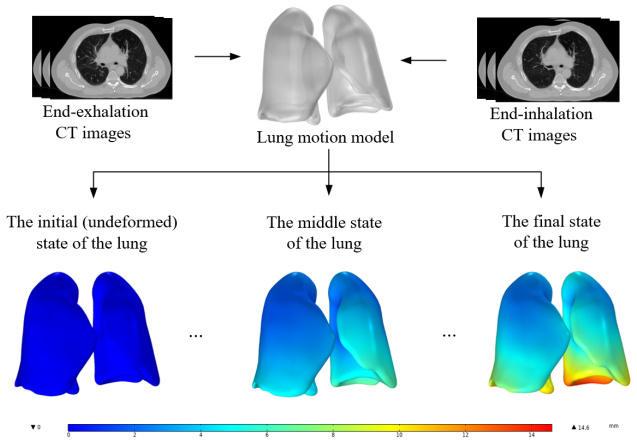

Fig. 4 The simulated dynamic states of the lung

2) Modeling Approach

For simplicity, the lung is modeled as linear, homogeneous, and isotropic elastic tissue, and only the lung expansion motion is simulated. Different values of biomechanical parameters are used in previous studies depending on the variations in simulation conditions. By referring to the study in [26], the Young's modulus E and Poisson's ratio v in this paper is fixed at 1 kPa and 0.3, respectively.

Root of the lung is supposed to be fixed, so the surface nodes in this area follow Dirichlet boundary conditions, and the other nodes in the deformed geometry follow the stress boundary conditions:

$$u(x) = 0, x \in \Gamma_{root} \cup \Gamma_{limiting} \tag{1}$$

$$\delta(x)n(x) = \left(P_{intrapl} + P_{contact}\right)n(x), x \in \Gamma_{deformed} \tag{2}$$

where $u(x)$ is the displacement vector at the point x. $\delta(x)$ and $n(x)$ is Cauchy stress and the outward pointing normal vector at the point x, respectively. The $P_{intrapl}$ represents the intrapleural pressure applied to the deformed surface. The $P_{contact}$ represent the contact pressure. The lung motion is modeled as a frictionless contact problem, which means:

$$\begin{gathered} g \geq 0 \\ P_{contact} \leq 0 \\ g \cdot P_{contact} = 0 \end{gathered} \tag{3}$$

where g denotes the gap between the deformed lung and the limiting geometry. When the gap is positive, the contact pressure is zero. Otherwise, the contact pressure is nonzero to prevent the expansion of the deformed lung.

By referring to the study in [21], estimated intrapleural pressure difference ΔP between the end-exhalation phase and the end-inhalation phase of each patient is calculated in equation (4):

$$\Delta P = \frac{V_l - V_i}{V_i} \cdot \frac{E}{3(1-2v)} \tag{4}$$

where V_l is the volume of the limiting lung geometry and V_i is the volume of the initial lung geometry. To make the deformed lung fully close to the end-inspiration geometry (i.e., reaching a volume ratio of at least 0.99), the applied intrapleural pressure will be adjusted accordingly.

As shown in Fig. 4, by building the lung motion model through this modeling approach, the whole dynamic lung motion during the inhalation can be simulated based on the CT images at the end-exhalation and end-inhalation moment.

C. Electrical Impedance Tomography

The 16-electrode EIT sensor is used in this work. The EIT sensor is placed between the 4th and 6th intercostal space [28]. The conventional adjacent protocol excitation strategy was

adopted, where a complete scan comprises 208 voltage measurements [29, 30]. The complete electrode model (CEM) is used to solve the forward model of EIT [31], which can be expressed as:

$$\nabla \cdot \left(\sigma(p)\nabla\phi(p)\right) = 0, p \in \Omega \tag{5}$$

$$\phi(p) + z_l\sigma(p)\frac{\partial\phi(p)}{\partial n} = U_l, p \in e_l, l = 1,2,\dots,L \tag{6}$$

$$\sigma(p)\frac{\partial\phi(p)}{\partial n} = 0, p \in \partial\Omega\backslash\bigcup_{l=1}^{L} e_l \tag{7}$$

$$\int_{e_l}\sigma(p)\frac{\partial\phi(p)}{\partial n} = I_l \tag{8}$$

$$\sum_{l=1}^{L} I_l = 0, \sum_{l=1}^{L} U_l = 0 \tag{9}$$

where the p is the point inside the sensing area Ω; $\phi(p)$ and $\sigma(p)$ denote the potential and conductivity at p respectively; z_l is the contact impedance between the electrodes and the body; n is outward unit normal vector to $\partial\Omega$; U_l and I_l is the electrical potential and injected current on the electrode e_l; L is the number of electrodes.

When the current is driven though the j-th pair of adjacent electrodes (e_j, e_{j+1}), the voltage difference between the k-th pair of adjacent electrodes (e_k, e_{k+1}) is:

$$\dot{U}^{j,k} = U_k^j - U_{k+1}^j \tag{10}$$

All the $\dot{U}^{j,k}$ for combinations of $j,k \in [1,\dots,16]$ and $j \neq k$ will be measured, and the convention $e_{17} = e_1$ is used.

The complete digital twin models can be built after combing the EIT sensing system with the numerical lung model. Thus, the electrical potential distribution of the dynamic lung model can be obtained. For instance, the electrical potential distributions of the model at the initial and final state of inhalation when the first electrode pair is excited are illustrated in Fig. 5.

Time-difference EIT is applied in this paper, so we use the difference between two complete measurements to reconstruct images:

$$\dot{\boldsymbol{U}} = \dot{\boldsymbol{U}}_t - \dot{\boldsymbol{U}}_{t_0} \tag{11}$$

where $\dot{\boldsymbol{U}}_t, \dot{\boldsymbol{U}}_{t_0} \in \mathbb{R}^{L(L-3)}$ is the complete measurements at time t and reference time (*i.e.,* end-exhalation) t_0 respectively.

For traditional EIT algorithms, the distribution of conductivity variation $\dot{\boldsymbol{G}}$ can be reconstructed by solving the inverse problem of EIT. This is usually formulated as an optimization problem:

$$\min_{\boldsymbol{G}}\left\{\|\dot{\boldsymbol{U}} - \boldsymbol{S}\dot{\boldsymbol{G}}\|^2 + \zeta \cdot l\left(\dot{\boldsymbol{G}}\right)\right\} \tag{12}$$

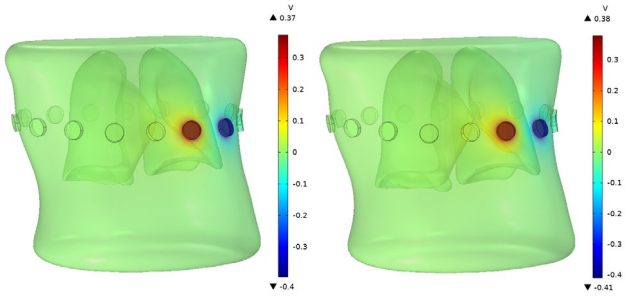

(a) (b)

Fig. 5 When the first electrode pair is excited, the electrical potential distribution of (a) the initial state of inhalation, (b) the final state of inhalation

where $\boldsymbol{S}$ is the sensitivity matrix; $l(\cdot)$ and $\zeta \in \mathbb{R}$ denote the regularization function and parameter, respectively. Many traditional algorithms have been applied to solve this problem, such as Newton–Raphson (NR) method [32]. When $l(\cdot)$ adopts Tikhonov regularization, the NR method can be described as:

$$\hat{\boldsymbol{G}}_{k+1} = \hat{\boldsymbol{G}}_k - (\boldsymbol{S}^T\boldsymbol{S} + \zeta\boldsymbol{I})^{-1}\boldsymbol{S}^T(\boldsymbol{S}\hat{\boldsymbol{G}}_k - \dot{\boldsymbol{U}}) \tag{13}$$

D. Image Reconstruction Network

U-Net has been developed for biomedical image segmentation, where it can work with few training images and yields more precise segmentations [33]. Based on the U-Net structure, we proposed an image reconstruction neural network (IR-Net), whose network structure is shown in Fig. 6. To better solve the specific problem in this paper, the downsampling steps and upsampling steps in the original U-Net architecture are reduced to three in the IR-Net to reduce network parameters and prevent overfitting.

The input of the IR-Net contains the two normalized EIT measurements using different normalization methods:

$$\boldsymbol{U}_{input1} = \frac{\dot{\boldsymbol{U}}}{\dot{\boldsymbol{U}}_{t_0}} \tag{14}$$

$$\boldsymbol{U}_{input2} = \frac{\dot{\boldsymbol{U}}}{\dot{\boldsymbol{U}}_{t_l} - \dot{\boldsymbol{U}}_{t_0}} \tag{15}$$

where $\dot{\boldsymbol{U}}_{t_l}$ is the EIT measurements at end-inhalation time t. The first channel of the input is $\boldsymbol{U}_{input1}$, which contains the conductivity variation information. Besides, for lung monitoring, the relative conductivity variation during the whole respiratory period is also important. So, the second channel of the network input is designed as $\boldsymbol{U}_{input2}$ to provide the relative conductivity variation information during the whole respiratory period. Because the second part of the input is susceptive to noises, the Sigmoid layer is used to reduce the influence of outliers. The fully connected (Fc) layer is used to obtain the initial images (64×64 pixels) from the two channels of input respectively. To demonstrate the effectiveness of adding $\boldsymbol{U}_{input2}$, the reconstructed results of the IR-Net with two-

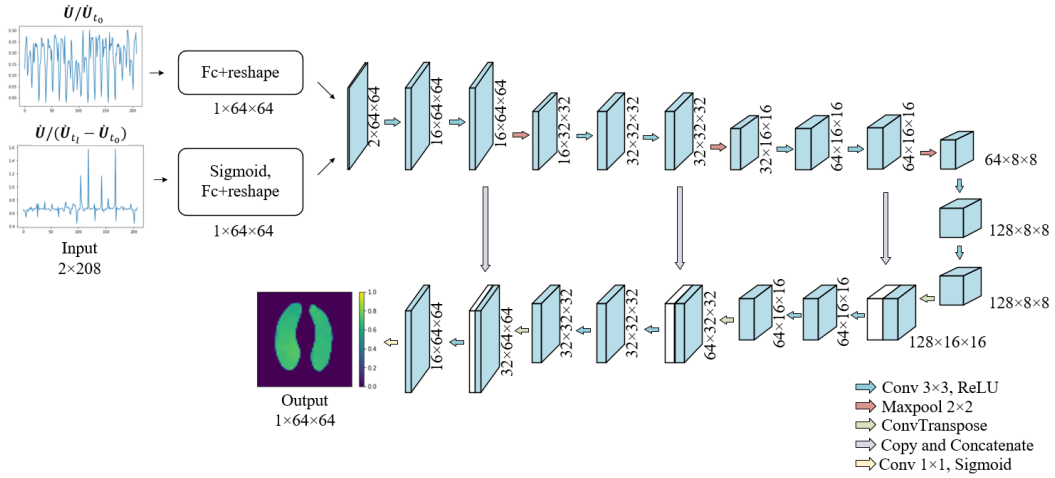

Fig. 6 The proposed image reconstruction network

channel input and IR-Net with only $\boldsymbol{U}_{input1}$ input (referred as modified U-Net) are listed in the section IV.

The U-Net structure is used to extract the features in initial images from Fc layer. The contracting path (at the top of Fig. 6) of the modified U-Net contains three downsampling steps. Every downsampling step consists of two 3×3 convolutions followed by a batch normalization layer and a rectified linear unit (ReLU). And the 2×2 max-pooling operation with stride 2 in each step is adopted to perform the downsampling. At each downsampling step, the number of feature channels is doubled. The expansive path (in the bottom side of Fig. 6) contains 3 upsampling steps and the feature maps from contracting path are concatenated by jump connections to provide additional information. At each upsampling step, 3 × 3 transposed convolution is utilized to double the size of feature maps and halve the feature channels. Finally, a 1×1 convolution layer is used to obtain the output reconstructed images. The conductivity variation in this paper is normalized in the range of [0,1], so Sigmoid is selected as the activation function for the final convolution layer to output the predicted images.

III. EXPERIMENTS SETUP

A. Dataset Collection

The 4D-Lung CT dataset used in this paper comes from the Cancer Imaging Archive (TCIA) [34]. This dataset consists of 20 patients (labeled from 100 to 119), and detailed information can be found in [35-37]. the image sets of patients 100-117 are used in this paper because the modeling method is not appropriate for the lung shape of the last two patients, whose lung has missing parts that may have resulted from surgical removal. Each CT image set has ten breathing phases (0 to 90%), among which the images at 0% (end-inhalation) and 50% phase (end-exhalation) are selected to model the respiratory motion.

In our lung motion model, the inhalation process is divided into 21 phases. The first phase, T_0, represents the end-exhalation state and the last phase, T_{20}, represents the end-inhalation state. The frequency of excitation current in EIT is 100 kHz, so the conductivity and relative permittivity of end-exhalation lung tissue is set as 0.26 *S/m* and 8531.4, respectively, whereas the conductivity and relative permittivity of end-inhalation lung tissue is set as 0.10 *S/m* and 4272.5, respectively [38]. The electrical properties of the deformed lung varied linearly with the volume change:

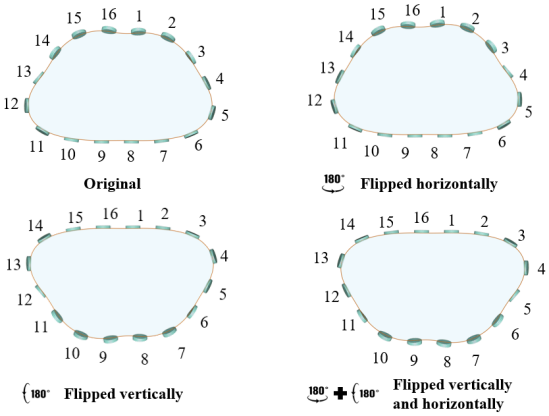

Fig. 7 Flip the original geometry to increase the amount of dataset

$$H_T = H_i + (H_l - H_i) * \frac{V_T - V_i}{V_l - V_i} \tag{16}$$

where H_T is the electrical property (conductivity and permittivity) at phase *T*. H_i and H_l are the electrical properties at the end-exhalation phase and the end-inhalation phase respectively. And V_T is the volume of the deformed lung at phase *T*.

The respiratory motion model of patients 100-112 are used to generate datasets for training the neural network. To increase the amount of data, the following methods are applied:

1) The electrode groups are placed on two different heights to measure the voltages, which is common in the real world because the electrode groups are not fixed on a specific height.
2) 5% Gaussian noise is added to the voltage measurements to improve the generalization of the proposed network.

TABLE I Image reconstruction results on the test set

Patient	115					116					117				
Phase	T_4	T_8	T_{12}	T_{16}	T_{20}	T_4	T_8	T_{12}	T_{16}	T_{20}	T_4	T_8	T_{12}	T_{16}	T_{20}
CT images	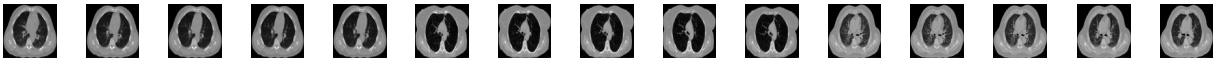														
Truth															
NR	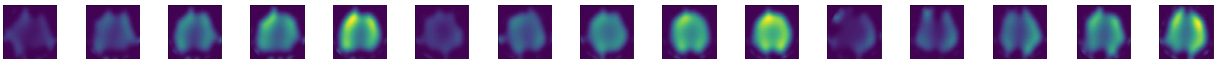														
CNN-RBF	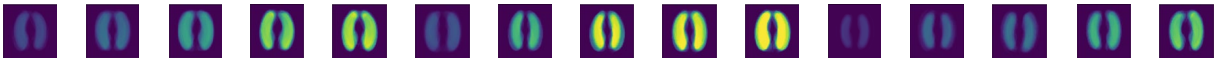														
Modified U-Net															
IR-Net															
IR-Net (Moved electrodes)															

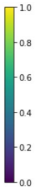

TABLE II Quantitative evaluation of prediction results of different algorithms on the test set

method	NR		CNN-RBF		modified U-Net		IR-Net	
	Noisy data	Noise-free	Noisy data	Noise-free	Noisy data	Noise-free	Noisy data	Noise-free
SSIM	0.368	0.444	0.666	0.686	0.725	0.783	0.764	0.811
RIE	0.748	0.567	0.479	0.430	0.503	0.424	0.459	0.383
CC	0.645	0.790	0.850	0.881	0.824	0.882	0.855	0.896
Time (ms)	7.27		6.90		6.17		6.41	

3) Flip the original geometry and corresponding labels horizontally or vertically (shown in Fig. 7).

After the data augmentation, the training dataset contains 4368 subsets finally. The data of patient 13-14 without flipping are used for validation, containing 168 subsets. And the images of patients 15-17 are used for testing, containing 252 subsets.

B. Evaluation Criteria

To quantitatively evaluate the reconstruction image quality, the Relative Image Error (RIE), Structural Similarity Index Measure (SSIM) [39] and Correlation Coefficient (CC) are employed. The RIE, SSIM and CC are defined as:

$$RIE = \frac{\|A - B\|_2}{\|B\|_2} \tag{17}$$

$$SSIM = \frac{(2\mu_A\mu_B + R_1)(2\delta_{AB} + R_2)}{(\mu_A^2 + \mu_B^2 + R_1)(\delta_A^2 + \delta_B^2 + R_2)} \tag{18}$$

$$CC = \frac{\delta_{AB}}{\delta_A \delta_B} \tag{19}$$

where A, B represent the reconstructed images and the true distribution, respectively; μ_A, μ_B, δ_A, δ_B, and δ_{AB} denote respectively the mean values, standard deviations, and covariance of images A, B; R_1, R_2 are the regularization constants for the luminance and contrast.

C. Network Training

Adam [40] is employed to optimize the network. The learning rate is 5×10^{-5}, and the number of training epoch is 1500. The networks are trained with a batch size of 128 on the Pytorch-GPU environment and implemented in NVIDIA GeForce RTX 3070 Ti Laptop GPU.

The mean square error (MSE) loss is exploited for optimization in the training:

$$L_{MSE} = \frac{1}{N}\sum_{n=1}^{N}\left\|F(I_n^i) - I_n^c\right\|_2^2 \tag{20}$$

where N is the number of training samples. $F(\cdot)$ is the nonlinear function representing the neural network. I_n^i is the EIT data and I_n^c is the corresponding labels.

TABLE III Quantitative evaluation of prediction results of IR-Net with different noise levels

Index	Noise levels			
	0%	3%	5%	10%
SSIM	0.811	0.782	0.764	0.737
RIE	0.383	0.434	0.459	0.522
CC	0.896	0.869	0.855	0.844

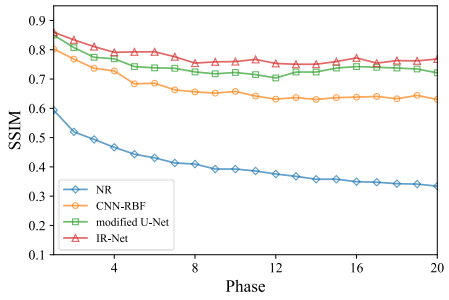

(a) SSIM of reconstructed results with respect to phases

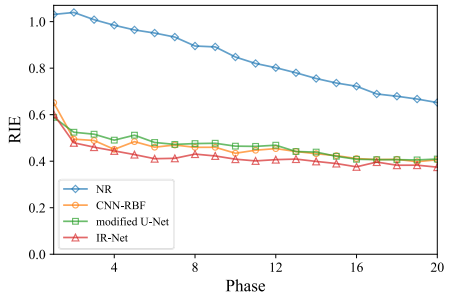

(b) RIE of reconstructed results with respect to phases

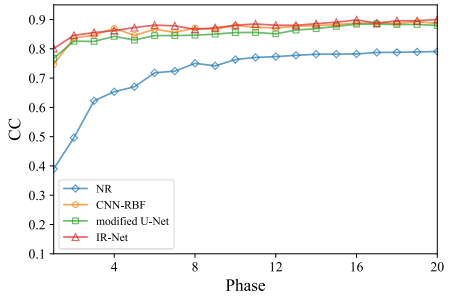

(c) CC of reconstructed results with respect to phases

Fig. 8 The performance of reconstructed results with respect to phases

IV. RESULTS AND DISCUSSIONS

Table I lists the predicted images from noisy data on the test set, and Table II shows the quantitative evaluation results. We also use the NR algorithm, CNN-RBF [41] and modified U-Net for comparison. The iteration number of NR algorithm is set to 10, and the training procedure of CNN-RBF and modified U-Net is the same as that of IR-Net.

As seen in Table I, the EIT images reconstructed by the NR algorithm have blurred boundaries and artifacts near the electrodes. Its performance is also easily affected by noise, as the SSIM of its reconstructed images decreases from 0.433 to 0.342 and the RIE increases from 0.565 to 0.676 when 5% Gaussian random noise is added. However, the results of the learning-based methods, which have utilized the proposed imaging framework, are greatly improved. The SSIM of the images reconstructed by learning-based methods are all above 0.66, and the RIE are all below 0.51. The learning-based methods can reconstruct conductivity distributions more accurately and has better anti-noise performance, demonstrating the feasibility of our proposed lung imaging framework. To further demonstrate the anti-noise performance of IR-Net, the quantitative evaluations of prediction results of IR-Net with different noise levels are listed in Table III. The noise levels of the EIT measurements are increased from 0 to 10%. As the noise increases, the SSIM declines from 0.811 to 0.737 and the CC decreases from 0.896 to 0.844, meanwhile, the RIE increases from 0.383 to 0.522. So, the effect of noise will be propagated from the EIT measurements to the results of IR-Net, but the performance of IR-Net at 10% Gaussian noise level in EIT measurements is still better than that of the other methods at 5% Gaussian noise level. Therefore, the IR-Net has better anti-noise performance. Besides, compared with CNN-RBF and modified U-Net with single input, $\boldsymbol{U}_{input1}$, IR-Net can better reconstruct the relative conductivity variation during the whole respiratory period because of the additional information in two-channel input. The imaging time of the four methods are close and have the potential to implement in real-time applications, as shown in the last row of Table II.

The average SSIM, RIE and CC of the reconstructed results for test data, including noisy data and noisy-free data, at every phase are plotted in Fig. 8. As shown in Fig. 8, the SSIM of the results reconstructed by NR algorithm declines during the inhalation process. The SSIM of images reconstructed by modified U-Net is better than that reconstructed by CNN-RBF, but CNN-RBF performance slightly better in RIE and CC index. And the results reconstructed by IR-Net are the best in all indexes. Through the IR-Net, the SSIM of the results can stay at around 0.8 during the whole inhalation process. And as shown in Fig. 8 (b), the RIE of the results reconstructed by IR-Net is much lower than that of reconstructed by NR algorithm while the CC index of IR-Net is much higher than that of NR algorithm as shown in Fig. 8 (c).

To further verify the practical ability of the proposed imaging framework, experimental data from [42] is tested. This EIT in vivo measurement was collected by Camille Gómez-Laberge on a normal human subject, but the way the electrodes were placed was different from the simulation data in this paper. In the experimental data, the first electrode is placed in the center of the sternum, while in the simulation data, the first and last electrodes are placed symmetrically around the sternum. To show the effectiveness of IR-Net, firstly we tested the reconstructed results of the simulation data of moved electrodes, and the corresponding electrode positions are shown in Fig. 9. The image results are in the last row of TABLE I. These results indicate that IR-Net can still accurately reconstruct the dynamic

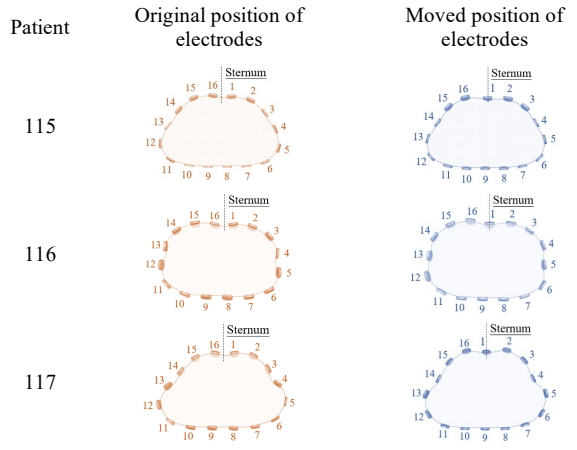

Fig. 9 The position of electrodes in our test dataset

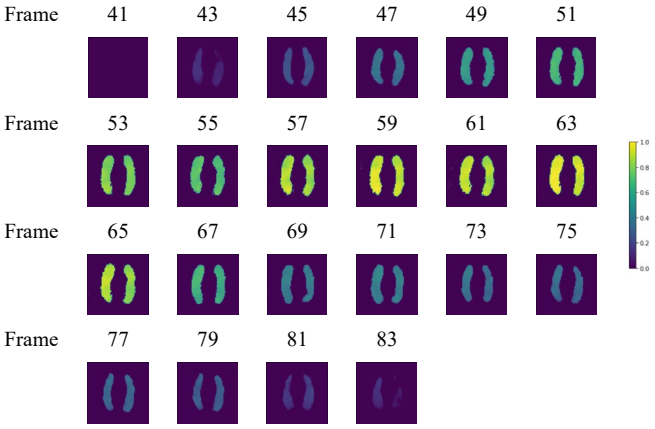

Fig. 10 Image reconstruction results of the experimental data

changes in lung conductivity when the electrode placement varies.

The reconstructed results of the first respiratory cycle (frame 41-83) in the data I.1 is shown in Fig. 10. Even though the corresponding CT images haven't been provided, the IR-Net can provide seemingly more accurate results to show the lung conductivity change during the dynamic respiratory process.

V. CONCLUSION

In this paper, we propose a novel imaging framework for lung EIT that leverages digital twin lung models to generate more data with accurate labels for deep learning. These models incorporate both biomechanical and electric field information to provide the geometry and electrical properties of the lung during respiration in simulation. Our proposed image reconstruction network can then learn from this prior information and output EIT images directly from voltage measurements. The effectiveness and feasibility of our framework were demonstrated using simulation and experimental data. Additionally, our framework is not patient-specific, meaning it can be trained on a number of digital twin models and applied to different patients. Our proposed imaging framework is currently a prototype and has been limited by the availability of CT data and patient tests. In the future, we plan to incorporate more accurate lung motion modeling methods and account for variations in electrical properties to improve the digital twin model. We also plan to expand our dataset to include a wider range of healthy and unhealthy lung cases with both CT and EIT measurements, in order to improve the generalization performance of our imaging framework.

REFERENCES

[1] L. Ball, V. Vercesi, F. Costantino, K. Chandrapatham, and P. Pelosi, "Lung imaging: how to get better look inside the lung," *Annals of translational medicine,* vol. 5, no. 14, 2017.

[2] T. Muders, H. Luepschen, and C. Putensen, "Impedance tomography as a new monitoring technique," *Current Opinion in Critical Care,* vol. 16, no. 3, pp. 269-275, Jun 2010, doi: 10.1097/MCC.0b013e3283390cbf.

[3] M. Kircher *et al.*, "Regional Lung Perfusion Analysis in Experimental ARDS by Electrical Impedance and Computed Tomography," *Ieee Transactions on Medical Imaging,* vol. 40, no. 1, pp. 251-261, Jan 2021, doi: 10.1109/tmi.2020.3025080.

[4] M. Zamani, M. Kallio, R. Bayford, and A. Demosthenous, "Generation of Anatomically Inspired Human Airway Tree Using Electrical Impedance Tomography: A Method to Estimate Regional Lung Filling Characteristics," *Ieee Transactions on Medical Imaging,* vol. 41, no. 5, pp. 1125-1137, May 2022, doi: 10.1109/tmi.2021.3136434.

[5] S. Liu, J. Jia, Y. D. Zhang, and Y. Yang, "Image reconstruction in electrical impedance tomography based on structure-aware sparse Bayesian learning," *IEEE transactions on medical imaging,* vol. 37, no. 9, pp. 2090-2102, 2018.

[6] S. Liu, Y. Huang, H. Wu, C. Tan, and J. Jia, "Efficient multitask structure-aware sparse Bayesian learning for frequency-difference electrical impedance tomography," *IEEE Transactions on industrial informatics,* vol. 17, no. 1, pp. 463-472, 2020.

[7] S. Liu, H. Wu, Y. Huang, Y. Yang, and J. Jia, "Accelerated structure-aware sparse Bayesian learning for three-dimensional electrical impedance tomography," *IEEE transactions on industrial informatics,* vol. 15, no. 9, pp. 5033-5041, 2019.

[8] S. J. Hamilton and A. Hauptmann, "Deep D-bar: Real-time electrical impedance tomography imaging with deep neural networks," *IEEE transactions on medical imaging,* vol. 37, no. 10, pp. 2367-2377, 2018.

[9] S. J. Hamilton, A. Hänninen, A. Hauptmann, and V. Kolehmainen, "Beltrami-net: domain-independent deep D-bar learning for absolute imaging with electrical impedance tomography (a-EIT)," *Physiological measurement,* vol. 40, no. 7, p. 074002, 2019.

[10] J. K. Seo, K. C. Kim, A. Jargal, K. Lee, and B. Harrach, "A Learning-Based Method for Solving III-Posed Nonlinear Inverse Problems: A Simulation

Study of Lung EIT," *Siam Journal on Imaging Sciences,* vol. 12, no. 3, pp. 1275-1295, 2019, doi: 10.1137/18m1222600.

[11] S. J. Ren, K. Sun, C. Tan, and F. Dong, "A Two-Stage Deep Learning Method for Robust Shape Reconstruction With Electrical Impedance Tomography (vol 69, pg 4887, 2020)," *Ieee Transactions on Instrumentation and Measurement,* vol. 69, no. 11, pp. 9284-9284, Nov 2020, doi: 10.1109/tim.2020.3012378.

[12] K. Zhang, R. Guo, M. Li, F. Yang, S. Xu, and A. Abubakar, "Supervised descent learning for thoracic electrical impedance tomography," *IEEE Transactions on Biomedical Engineering,* vol. 68, no. 4, pp. 1360-1369, 2020.

[13] Z. Lin *et al.*, "Feature-Based Inversion Using Variational Autoencoder for Electrical Impedance Tomography," *IEEE Transactions on Instrumentation and Measurement,* vol. 71, pp. 1-12, 2022.

[14] X. Zhang *et al.*, "V-Shaped Dense Denoising Convolutional Neural Network for Electrical Impedance Tomography," *IEEE Transactions on Instrumentation and Measurement,* vol. 71, pp. 1-14, 2022.

[15] Z. Wei and X. Chen, "Induced-current learning method for nonlinear reconstructions in electrical impedance tomography," *IEEE transactions on medical imaging,* vol. 39, no. 5, pp. 1326-1334, 2019.

[16] Q. Wang *et al.*, "Exploring Respiratory Motion Tracking Through Electrical Impedance Tomography," *Ieee Transactions on Instrumentation and Measurement,* vol. 70, 2021, Art no. 4504712, doi: 10.1109/tim.2021.3083892.

[17] G. Coorey, G. A. Figtree, D. F. Fletcher, and J. Redfern, "The health digital twin: advancing precision cardiovascular medicine," *Nature Reviews Cardiology,* vol. 18, no. 12, pp. 803-804, 2021.

[18] B. Björnsson *et al.*, "Digital twins to personalize medicine," *Genome medicine,* vol. 12, no. 1, pp. 1-4, 2020.

[19] M. N. Kamel Boulos and P. Zhang, "Digital twins: from personalised medicine to precision public health," *Journal of Personalized Medicine,* vol. 11, no. 8, p. 745, 2021.

[20] S. Wang *et al.*, "A digital twin of electrical tomography for quantitative multiphase flow imaging," *Communications Engineering,* vol. 1, no. 1, p. 41, 2022.

[21] R. Werner, J. Ehrhardt, R. Schmidt, and H. Han De Ls, "Patient-specific finite element modeling of respiratory lung motion using 4D CT image data," *Medical Physics,* vol. 36, 2009.

[22] B. Fuerst *et al.*, "Patient-Specific Biomechanical Model for the Prediction of Lung Motion From 4-D CT Images," *IEEE Transactions on Medical Imaging,* vol. 34, no. 2, p. 599, 2015.

[23] H. Ladjal, M. Beuve, P. Giraud, and S. Behzad, "Towards Non-invasive Lung Tumor Tracking Based on Patient-Specific Model of Respiratory System," *IEEE Transactions on Biomedical Engineering,* vol. PP, no. 99, 2021.

[24] P. Alvarez, S. Rouzé, M. I. Miga, Y. Payan, and M. Chabanas, "A hybrid, image-based and biomechanics-based registration approach to markerless intraoperative nodule localization during video-assisted thoracoscopic surgery," *Medical Image Analysis,* vol. 69, no. 1, p. 101983, 2021.

[25] L. Han, H. Dong, J. R. McClelland, L. Han, D. J. Hawkes, and D. C. Barratt, "A hybrid patient-specific biomechanical model based image registration method for the motion estimation of lungs," *Medical image analysis,* vol. 39, pp. 87-100, 2017.

[26] R. Werner, J. Ehrhardt, R. Schmidt, and H. Handels, "Modeling respiratory lung motion: a biophysical approach using finite element methods," *Proceedings of SPIE - The International Society for Optical Engineering,* vol. 6916, 2008.

[27] A. Fedorov *et al.*, "3D Slicer as an image computing platform for the Quantitative Imaging Network," *Magnetic Resonance Imaging,* vol. 30, no. 9, pp. 1323-1341, 2012.

[28] PulmoVista 500 Basics Getting Started [Online] Available: https://www.draeger.com/Products/Content/PulmoVista%20500%20SW1.30-%20BASICS_Getting_Started.pdf

[29] B. H. Brown and A. D. Seagar, "The Sheffield data collection system," *Clinical Physics and Physiological Measurement,* 1987.

[30] K. S. Jin, C. K. Kang, A. Jargal, K. Lee, and B. Harrach, "A Learning-Based Method for Solving Ill-Posed Nonlinear Inverse Problems: A Simulation Study of Lung EIT," *SIAM Journal on Imaging Sciences,* vol. 12, no. 3, pp. 1275-1295, 2019.

[31] K. S. Cheng and D. Isaacson, "Electrode models for electric current computed tomography," *Biomedical Engineering IEEE Transactions on,* vol. 36, no. 9, pp. 918-924, 1989.

[32] W. Yang and L. Peng, "Image reconstruction algorithms for electrical capacitance tomography," *Measurement science and technology,* vol. 14, no. 1, p. R1, 2002.

[33] O. Ronneberger, P. Fischer, and T. Brox, "U-net: Convolutional networks for biomedical image segmentation," in *International Conference on Medical image computing and computer-assisted intervention*, 2015: Springer, pp. 234-241.

[34] K. Clark *et al.*, "The Cancer Imaging Archive (TCIA): Maintaining and Operating a Public Information Repository," *Journal of Digital Imaging,* vol. 26, no. 6, pp. 1045-1057, Dec 2013, doi: 10.1007/s10278-013-9622-7.

[35] G. D. Hugo *et al.*, "A longitudinal four-dimensional computed tomography and cone beam computed tomography dataset for image-guided radiation therapy research in lung cancer," *Medical physics,* vol. 44, no. 2, pp. 762-771, 2017.

[36] N. O. Roman, W. Shepherd, N. Mukhopadhyay, G. D. Hugo, and E. Weiss, "Interfractional positional variability of fiducial markers and primary tumors in locally advanced non-small-cell lung cancer during audiovisual biofeedback radiotherapy," *International Journal of Radiation Oncology* Biology* Physics,* vol. 83, no. 5, pp. 1566-1572, 2012.

[37] S. Balik *et al.*, "Evaluation of 4-dimensional computed tomography to 4-dimensional cone-beam computed tomography deformable image registration for lung cancer adaptive radiation therapy," *International Journal of Radiation Oncology* Biology* Physics,* vol. 86, no. 2, pp. 372-379, 2013.

[38] D. Chakraborty and M. Chattopadhyay, "Monitoring of the Lung Fluid Movement and Estimation of Lung Area Using Electrical Impedance Tomography," in *Next Generation Sensors and Systems*, vol. 16, S. C. Mukhopadhyay Ed., (Smart Sensors Measurement and Instrumentation, 2016, pp. 161-190.

[39] Z. Wang, A. C. Bovik, H. R. Sheikh, and E. P. Simoncelli, "Image quality assessment: from error visibility to structural similarity," *IEEE transactions on image processing,* vol. 13, no. 4, pp. 600-612, 2004.

[40] D. P. Kingma and J. Ba, "Adam: A method for stochastic optimization," *arXiv preprint arXiv:1412.6980,* 2014.

[41] Y. Wu *et al.*, "Shape reconstruction with multiphase conductivity for electrical impedance tomography using improved convolutional neural network method," *IEEE sensors journal,* vol. 21, no. 7, pp. 9277-9287, 2021.

[42] A. Adler and W. R. Lionheart, "Uses and abuses of EIDORS: an extensible software base for EIT," *Physiological measurement,* vol. 27, no. 5, p. S25, 2006.